Combined Active Flux and High Frequency Injection Methods for Sensorless Direct Flux Vector Control of Synchronous Reluctance Machines

Combined Active Flux and High-Frequency Injection Methods for Sensorless Direct-Flux Vector Control of Synchronous Reluctance Machines

Arzhang Yousefi-Talouki, Paolo Pescetto, Gianmario Pellegrino, *Senior Member, IEEE*, and Ion Boldea, *Life Fellow, IEEE*

***Abstract*—This paper proposes a sensorless control scheme for synchronous reluctance (SyR) motor drives based on the direct-flux vector control (DFVC) method. The control operates in stator-flux-oriented coordinates, using constant switching frequency. A hybrid position and speed observer is proposed, based on the combination of the active flux concept and high-frequency signal injection and demodulation. The two methods are fused together to form a unique position and speed estimate signals, with seamless transition between the two models based on reference speed. The proposed observer covers a wide speed range, from standstill operation at full load to flux weakening (FW). Furthermore, it is inherently immune from position estimation error caused by cross saturation, as proven mathematically and experimentally. The motor is operated according to the maximum torque per ampere (MTPA) law. Specific issues related to MTPA around zero torque are addressed in this paper. The proposed control technique extends the range of application of the DFVC to encoderless drives, and can be usefully adopted in those applications where both zero-speed and FW speed range operations are necessary, such as home appliances, or automotive and aerospace actuators and generators. A 2.2-kW SyR motor prototype was tested to verify the feasibility of the proposed method. Key tuning aspects are addressed in this paper.**

***Index Terms*—Active flux, direct-flux vector control (DFVC), high-frequency (HF) injection, sensorless control, synchronous reluctance (SyR) machines.**

I. Introduction

SYNCHRONOUS reluctance (SyR) motors have become popular thanks to their prominent features, such as efficiency, good torque density, and replacement of induction motors with minimum modifications of manufacturing process [1]–[3]. Moreover, as the price of rare-earth materials used in permanent-magnet (PM) machines is uncertain, the SyR motor can be a cost-effective solution to all PM motor counterparts. Finally, SyR motors are salient by definition, and, therefore, compatible with position sensorless methods based on saliency tracking.

The direct torque control (DTC) method has attracted the attention of many researchers and engineers due to its fast dynamic response and robust implementation [4]–[7]. The two major shortcomings of this method are the variable switching frequency and the high torque ripple. The direct-flux vector control (DFVC) method [8]–[10] retains the basic advantages of the DTC, with the additional features of using constant switching frequency and explicit limitation of the current vector amplitude. The DFVC controls the amplitude of the stator flux linkage and the torque current component via two proportional-integral (PI) regulators, using the stator-flux-oriented coordinates d_s, q_s defined in Fig. 1. As for DTC, the voltage-limited speed region is easily exploited by directly handling the flux linkage amplitude in flux-weakening (FW) mode.

Conventionally, synchronous motor drives use a shaft encoder for sensing the rotor position. Numerous sensorless control techniques were developed during the last decades, for eliminating the encoder. Although both the DTC and DFVC use the stator flux axes d_s, q_s instead of the rotor synchronous axes d, q, they still need the knowledge of the rotor position, in particular, when torque control is required at standstill [6]. Sensorless control schemes are divided in the two main categories of the ones relying on motional back electromotive force (EMF) [11]–[13] and the ones tracking the magnetic saliency of the rotor [6]–[14], i.e., by injecting additional high-frequency (HF) signals into the machine. Very often, the two methods are combined to include the standstill operating region [15]–[17]. Examples of sensorless DTC for interior PM and PM-assisted machines are in [6] and [18]–[21]. Morales-Caporal and Pacas [22] propose a sensorless predictive DTC method for a SyR motor, extracting the rotor position through pulse width modulation (PWM) modification. However, the performance of the drive at high speed and the transition between high-speed and low-speed regions is not clearly shown. A hybrid active flux and HF injection method was proposed in [23] for sensorless vector control of an axially laminated SyR motor. Using the active flux observer, the sensorless controller operates appropriately at very low-speed levels down to 2 r/min. A sensorless vector control was proposed in [24], combining the HF injection with adaptive observer for SyR motors. In every abovementioned paper on SyR motors,

Manuscript received September 21, 2016; revised December 5, 2016 and February 16, 2017; accepted April 9, 2017. Date of publication April 24, 2017; date of current version December 1, 2017. Recommended for publication by Associate Editor J. O. Ojo. *(Corresponding author: Arzhang Yousefi-Talouki.)*

A. Yousefi-Talouki, P. Pescetto, and G. Pellegrino are with the Department of Energy, Politecnico di Torino, Turin 10129, Italy (e-mail: arzhang.yousefitalouki@polito.it; paolo.pescetto@polito.it; gianmario.pellegrino@polito.it).

I. Boldea is with the Department of Electrical Machines and Drives, University Politehnica of Timisoara, Timisoara 300006, Romania (e-mail: ion.boldea@upt.ro).

Color versions of one or more of the figures in this paper are available online at http://ieeexplore.ieee.org.

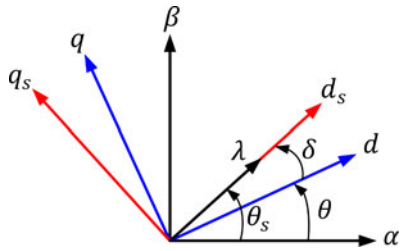

Fig. 1. Reference frames: Stator (α, β), rotor (d, q), and stator flux (d_s, q_s) coordinates.

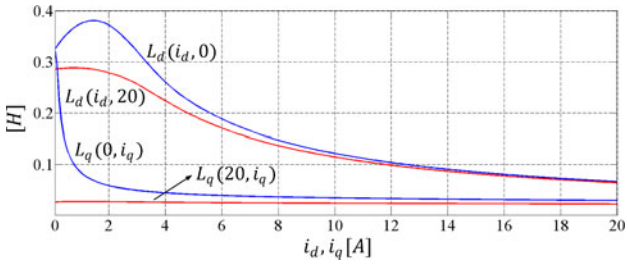

Fig. 2. Flux-linkage maps of the 2.2-kW SyR motor under test, evaluated experimentally (ratings in Table I).

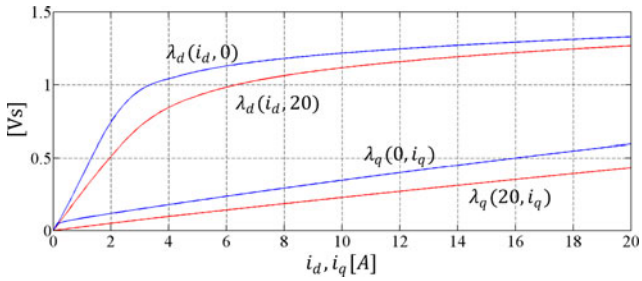

Fig. 3. dq inductances of the 2.2-kW SyR motor under test derived from flux-linkage maps.

maximum torque per ampere (MTPA) strategy was not used and a constant d-axis current was injected in the whole torque operating range. This is due to a specific issue in SyR motors: both saliency-based and model-based position estimations tend to fail around zero torque [25]. Dealing with the DFVC method, to the best knowledge of the authors, there are only a few papers hitherto reporting the combination of this method with sensorless applications [26], [27], however not in a wide speed range.

This paper proposes a sensorless DFVC technique for SyR motor drives. The proposed method uses alternated HF signal injection in combination with the active flux concept to build the rotor position estimate in a wide speed range including standstill and FW. In spite of commonly used current demodulation, flux estimate signal is demodulated to track the rotor position in the speed area covered by the signal injection. This inherently avoids the occurrence of position error due to cross saturation. Moreover, it will be discussed extensively that sensorless control for SyR motors is impossible at zero current. In this condition, both model-based and saliency-based position estimation fail. Hence, an appropriate minimum flux excitation is proposed at low torque, while for medium and high load, the sensorless control operates based on MTPA. Experimental results show that the steady-state position error is zero at all speed and torque levels and under control during speed transients, and that the transition between the two estimation methods is seamless and reversible. A transparent tuning methodology for the observer and the low-speed and high-speed models fusion is provided, and the effect of parameters put in evidence. Also, FW operation is documented experimentally. Finally, performance comparison with one popular HF voltage injection-current demodulation sensorless method [24] is provided in experiments to further investigate the effect of cross saturation. The proposed control technique is a solid candidate for general purpose control of SyR motor drives, without the need of a shaft encoder.

II. Direct-Flux Vector Control

The DFVC technique presented in [8] is briefly described in this section. The rotor and stator flux reference frames are illustrated in Fig. 1, where (α, β), (d, q), and (d_s, q_s) stand for stationary frame, rotor flux frame, and stator -flux frame, respectively.

A. Motor Model in Rotor Coordinates

The model of a SyR motor in rotor reference frame is expressed in (1)–(3), where R_s is the stator resistance, λ_d and λ_q are stator flux linkages, p is the pole pairs, T stands for electromagnetic torque, and L_d, L_q are the d, q inductances

$$\begin{cases} v_d = R_s i_d + \dfrac{d\lambda_d}{dt} - \omega\lambda_q \\ v_q = R_s i_q + \dfrac{d\lambda_q}{dt} + \omega\lambda_d \end{cases} \tag{1}$$

$$T = \frac{3}{2} \cdot p \cdot (\lambda_d i_q - \lambda_q i_d) \tag{2}$$

$$\begin{cases} \lambda_d = \lambda_d(i_d, i_q) = L_d(i_d, i_q) \cdot i_d \\ \lambda_q = \lambda_q(i_d, i_q) = L_q(i_d, i_q) \cdot i_q \end{cases} . \tag{3}$$

The current-to-flux-linkage maps (3) include saturation and cross saturation effects. The flux-linkage maps and apparent inductances versus current component in d, q rotor frame for the motor under test are reported in Figs. 2 and 3, respectively. The flux maps can be also identified automatically using sensorless self-commissioning methods as addressed in [28].

B. Motor Model in Flux Coordinates

The voltage equation (1) is rotated to the stator-flux-oriented reference frame $d_s q_s$, defined in Fig. 1, and (4) is obtained. By definition of flux-oriented frame, the flux components in $d_s q_s$ are $\lambda_{ds} = \lambda$ and $\lambda_{qs} = 0$, being λ the stator flux amplitude. The angle δ is the flux phase angle respect to the rotor direct axis d

$$\begin{cases} v_{ds} = R_s i_{ds} + \dfrac{d\lambda_{ds}}{dt} - \left(\omega + \dfrac{d\delta}{dt}\right)\lambda_{qs} = R_s i_{ds} + \dfrac{d\lambda}{dt} \\ v_{qs} = R_s i_{qs} + \dfrac{d\lambda_{qs}}{dt} + \left(\omega + \dfrac{d\delta}{dt}\right)\lambda_{ds} = R_s i_{qs} + \lambda\left(\omega + \dfrac{d\delta}{dt}\right) \end{cases} . \tag{4}$$

To express the electromagnetic torque as a function of the flux vector amplitude λ and phase δ, the torque equation in dq components (2) is manipulated substituting $\lambda_d = \lambda \cdot \cos(\delta)$ and

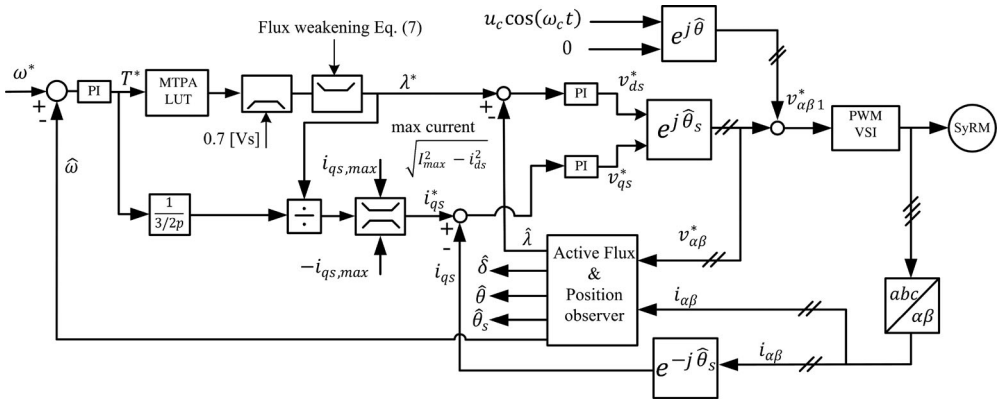

Fig. 4. Sensorless DFVC scheme.

$\lambda_q = \lambda \cdot \sin(\delta)$. The torque equation in the new form is

$$T = \frac{3}{2} \cdot p \cdot \frac{L_d - L_q}{2L_d L_q} \cdot \lambda^2 \cdot \sin(2\delta). \tag{5}$$

Alternatively, the simpler torque expression (6) can be obtained via the cross product of the flux linkage and current vectors, expressed in $d_s q_s$ coordinates, remembering that $\lambda_{ds} = \lambda$ and $\lambda_{qs} = 0$

$$T = \frac{3}{2} \cdot p \cdot (\lambda_{ds} i_{qs} - \lambda_{qs} i_{ds}) = \frac{3}{2} \cdot p \cdot \lambda \cdot i_{qs}. \tag{6}$$

Equation (6) is the core of the DFVC strategy, where torque is controlled via λ and i_{qs}.

C. DFVC Scheme

The block diagram of the sensorless DFVC for a speed-controlled SyR motor drive is illustrated in Fig. 4. The stator flux amplitude λ and the i_{qs} current component are closed-loop controlled using PI regulators. The stator flux is regulated by means of d_s-axis channel, while i_{qs} is dynamically coupled with flux control axis, as shown in [8]. However, this disturbance effect can be model-based compensated, if needed. The flux feedback $\hat{\lambda}$ is acquired from the flux observer. For the sake of efficiency, MTPA trajectory is adopted which correlates the flux amplitude to the desired torque set points. The flux amplitude reference is lower limited to 0.7 Vs both to ensure a minimum level of back-EMF excitation and to make saliency-based position tracking possible as explained in the following. The quadrature current reference i_{qs}^* is calculated according to torque and flux set points using the inverse of (6). $\hat{\theta}$ and $\hat{\omega}$ in Fig. 4 are the observed rotor position and speed signals coming from the sensorless position observer.

Over a certain speed, the control switches to FW mode to comply with the maximum voltage limitation of the inverter. The maximum voltage limit is respected by limiting the flux reference as

$$\lambda^* \leq \frac{[V_{\max} - R_s \cdot i_{qs} \cdot \mathrm{sign}(\hat{\omega})]}{|\hat{\omega}|} \tag{7}$$

where $V_{\max} = v_{\mathrm{dc}}/\sqrt{3}$ and v_{dc} is the dc-link voltage measurement. The FW block is independent from motor parameters, with the exception of R_s.

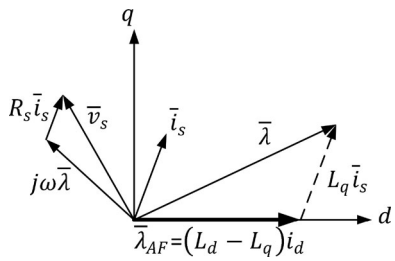

Fig. 5. Active flux vector diagram in *dq* frame.

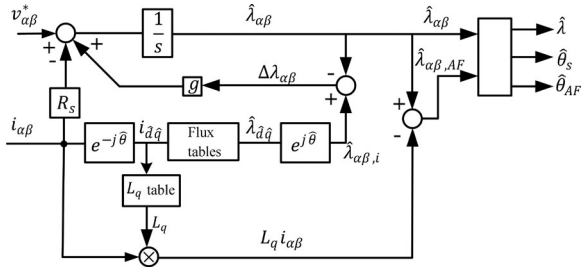

Fig. 6. Stator flux and active flux observer diagram.

III. Sensorless Active Flux Observer

The active flux concept was proposed for the first time in [29], turning salient-pole ac machines into fictitious nonsalient-pole ones. The dq components of active flux vector ($\bar{\lambda}_{AF}$) are expressed as (8). As can be seen, the active flux vector lies in rotor *d*-axis since the *q*-axis component is zero. Hence, position of active flux vector is identical to the rotor position. Fig. 5 shows the active flux concept graphically, where $\bar{\lambda}$ and $\bar{i}_s$ are the stator flux linkage and stator current, respectively.

$$\begin{cases} \lambda_{dAF} = \lambda_d - L_q \cdot i_d = (L_d - L_q)\, i_d = \bar{\lambda}_{AF} \\ \lambda_{qAF} = \lambda_q - L_q \cdot i_q = 0 \end{cases}. \tag{8}$$

The flux observer illustrated in Fig. 6 is based on back-EMF integration (voltage model) and a compensation signal coming from the error between the observed flux $\hat{\lambda}_{\alpha\beta}$ and a second flux estimate $\hat{\lambda}_{\alpha\beta,i}$ obtained from the current vector through dq flux tables (current model). The observer's transfer function (9) shows that the scalar feedback gain of the observer *g* rad/s

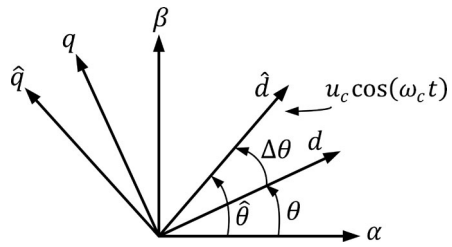

Fig. 7. Actual and estimated rotor reference frame.

is the crossover angular frequency between the voltage and current models

$$\hat{\lambda}_{\alpha\beta} = \frac{s}{s+g}\left(\frac{v^*_{\alpha\beta} - R_s i_{\alpha\beta}}{s}\right) + \frac{g}{s+g}\left(\hat{\lambda}_{\alpha\beta,i}\right). \tag{9}$$

The current model dominates at low-frequency levels ($\omega < g$), whereas the observed flux comes from the voltage model at higher frequency ($\omega > g$). The stator flux direction is obtained as

$$\sin\left(\hat{\theta}_s\right) = \frac{\hat{\lambda}_\beta}{\sqrt{\hat{\lambda}^2_\alpha + \hat{\lambda}^2_\beta}},\ \cos\left(\hat{\theta}_s\right) = \frac{\hat{\lambda}_\alpha}{\sqrt{\hat{\lambda}^2_\alpha + \hat{\lambda}^2_\beta}}\ . \tag{10}$$

The active flux (8) is evaluated in Fig. 6 using the offline calculated L_q table, obtained from the flux tables of the motor. Fig. 3 reports the L_q values as a function of i_q with i_d as parameter. Active flux position coordinates are finally calculated as

$$\begin{cases} \sin\left(\hat{\theta}_{AF}\right) = \dfrac{\hat{\lambda}_{\beta,AF}}{\left|\hat{\lambda}_{AF}\right|} = \dfrac{\hat{\lambda}_{\beta,AF}}{\sqrt{\hat{\lambda}^2_{\alpha,AF} + \hat{\lambda}^2_{\beta,AF}}} \\ \cos\left(\hat{\theta}_{AF}\right) = \dfrac{\hat{\lambda}_{\alpha,AF}}{\left|\hat{\lambda}_{AF}\right|} = \dfrac{\hat{\lambda}_{\alpha,AF}}{\sqrt{\hat{\lambda}^2_{\alpha,AF} + \hat{\lambda}^2_{\beta,AF}}} \end{cases}. \tag{11}$$

A. HF Signal Injection and Demodulation

To estimate the rotor position at low speed and standstill, conventionally a HF voltage is injected on estimated rotor $\hat{d}$-axis and HF current response in quadrature axis is demodulated. However, it was shown in [30] that demodulation of $\hat{q}$-axis current component presents a position estimation error due to the cross saturation. In this paper, instead of commonly used current demodulation, the output of flux tables in flux observer ($\hat{\lambda}_{\hat{q},i}$) is demodulated. It will be shown mathematically that the proposed demodulation technique is immune from cross saturation error. The amplitude and frequency of HF injected voltage are 50 V, and 833 Hz, respectively.

When a HF voltage is injected to the $\hat{d}$-axis, the HF current responses are as (12), where u_c is the amplitude of the injected voltage and ω_c is the carrier frequency. Subscript *HF* shows the high-frequency components and $\Delta\theta = \hat{\theta} - \theta$ is the rotor position error. L_{dd} and L_{qq} are incremental inductances. Also, L_{dq} stands for mutual inductance. Fig. 7 illustrates the actual and estimated rotor frame and HF injection

$$\begin{cases} I_{\hat{d}HF} = B \cdot [L_{\rm cm} - L_{\rm dm}\cos\left(2\Delta\theta\right) - L_{dq}\sin\left(2\Delta\theta\right)] \\ I_{\hat{q}HF} = B \cdot [L_{\rm dm}\sin\left(2\Delta\theta\right) - L_{dq}\cos\left(2\Delta\theta\right)] \end{cases} \tag{12}$$

$$\begin{cases} B\left(i_d, i_q\right) = \dfrac{u_c \sin\left(\omega_c t\right)}{\omega_c\left(L_{dd}L_{qq} - L^2_{dq}\right)} \\ L_{cm} = \dfrac{L_{dd} + L_{qq}}{2},\quad L_{dm} = \dfrac{L_{dd} - L_{qq}}{2} \end{cases}. \tag{13}$$

It is seen from (3) that using flux tables and estimated current components ($I_{\hat{d}HF},\ I_{\hat{q}HF}$), HF flux component is obtained as (14). Subscript *i* means the flux components coming from flux tables (current model)

$$\begin{bmatrix} \hat{\lambda}_{\hat{d}HF,i} \\ \hat{\lambda}_{\hat{q}HF,i} \end{bmatrix} = \begin{bmatrix} L_{dd} & L_{dq} \\ L_{dq} & L_{qq} \end{bmatrix} \cdot \begin{bmatrix} I_{\hat{d}HF} \\ I_{\hat{q}HF} \end{bmatrix}. \tag{14}$$

With replacing (12) in (14), it is deduced that

$$\begin{cases} \hat{\lambda}_{\hat{d}HF,i} = B[L_{dd}L_{\rm cm} - (L_{dd}L_{\rm dm})\cos\left(2\Delta\theta\right) \\ \qquad\qquad -L_{dq}L_{\rm cm}\sin\left(2\Delta\theta\right)] \\ \hat{\lambda}_{\hat{q}HF,i} = B[L_{dq}L_{\rm cm}[1 - \cos\left(2\Delta\theta\right)] \\ \qquad\qquad +[L_{qq}L_{\rm dm} - L^2_{dq}]\sin\left(2\Delta\theta\right)] \end{cases}. \tag{15}$$

For small values of $\Delta\theta$, the term $[1 - \cos(2\Delta\theta)]$ in $\hat{\lambda}_{\hat{q}HF,i}$ is negligible. Hence, $\hat{\lambda}_{\hat{q}HF,i}$ is approximated as

$$\hat{\lambda}_{\hat{q}HF,i} \cong B \cdot \left[L_{qq}L_{\rm dm} - L^2_{dq}\right] \cdot \sin\left(2\Delta\theta\right). \tag{16}$$

$\hat{\lambda}_{\hat{q}HF,i}$ signal (16) is closed-loop controlled to track the rotor position. With reference to Fig. 8, $\hat{\lambda}_{\hat{q},i}$ signal is initially bandpass filtered. The resulting signal $\hat{\lambda}_{\hat{q}HF,i}$ is demodulated and low-pass filtered (LPF). Finally, the position error feedback ϵ (17) is obtained

$$\epsilon = \mathrm{LPF}\left[\hat{\lambda}_{\hat{q}HF,i} \cdot \sin\left(\omega_c t\right)\right]. \tag{17}$$

Manipulating (16) and (17), the position error is put in evidence as

$$\epsilon = \frac{u_c}{2\omega_c} \cdot \frac{L_{qq}L_{\rm dm} - L^2_{dq}}{L_{dd}L_{qq} - L^2_{dq}} \cdot \sin\left(2\Delta\theta\right) \cong k_\epsilon \cdot \Delta\theta \tag{18}$$

where k_ϵ is as

$$k_\epsilon\left(i_d, i_q\right) = \frac{u_c}{\omega_c} \cdot \frac{L_{qq}L_{dm} - L^2_{dq}}{L_{dd}L_{qq} - L^2_{dq}}. \tag{19}$$

The demodulated error signal (18) is input into a PI regulator and fed back to the control to force it to zero in closed loop. Fig. 9 shows the tracking loop used for rotor position estimation where $\hat{\omega}_{HF}$ stands for observed speed obtained from HF injection technique.

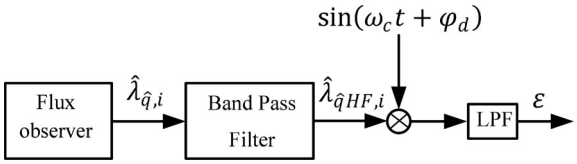

Fig. 8. HF injection-based demodulation process. φ_d is for compensation of discretization delay.

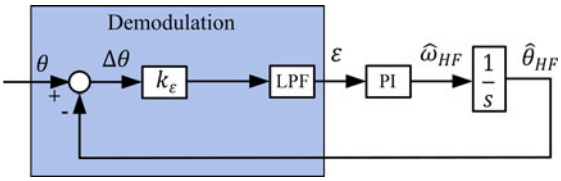

Fig. 9. HF injection-based tracking loop.

B. Absence of Cross Saturation Error

As said, the cross saturation effect is inherently overcome if the q-axis flux component (16) is used in the position tracking loop. Equation (16) shows that $\hat{\lambda}_{\hat{q}HF,i}$ is proportional to the position error ($\Delta\theta$), and, thus, the tracking loop will converge to the correct rotor position ($\Delta\theta = 0$) when $\hat{\lambda}_{\hat{q}HF,i}$ is forced to zero. Conversely, if $I_{\hat{q}HF}$ (12) were demodulated in place of $\hat{\lambda}_{\hat{q}HF,i}$, the tracking loop would converge to a steady-state position error $\Delta\theta_{dq}$, expressed in (20). According to (12), $\Delta\theta = 0$ is not a solution for equation $I_{\hat{q}HF} = 0$

$$\Delta\theta_{dq} = \frac{1}{2}\arctan\left(\frac{2L_{dq}}{L_{dd} - L_{qq}}\right). \tag{20}$$

C. Effect of HF Injection on the Observed Flux

Measured currents $i_{\alpha\beta}$ contain an HF component, as said. However, they are not LPF when used for control or flux estimation purposes. Looking at the flux observer scheme in Fig. 6, (9) suggests that the flux observer is a high-pass filter for the back-EMF signals, and a low-pass filter with cutoff frequency g for the current-model-based flux estimate. Therefore, the impact of HF noise of the observer's input ($i_{\alpha\beta}$) on the back-EMF term is minor, because limited to the resistance voltage component, and it is inherently LPF in the current model branch of the observer. The other observer's input is $v^*_{\alpha\beta}$, that is sampled before HF injection, as evidenced in Fig. 4. As a consequence, the observed flux is not affected by HF oscillation.

D. Tuning of the Tracking Loop

Fig. 10 shows k_ϵ for different working points of the motor under test. It is seen that the critical area is around no load condition ($i_q = 0$) when the sign of k_ϵ changes. As introduced in Section II-C, the flux amplitude reference is set according to the MTPA law, and lower bounded to 0.7 Vs. This guarantees a minimum level of excitation to the motor, and approximately corresponds to the condition $i_d = 2$ A highlighted in green in

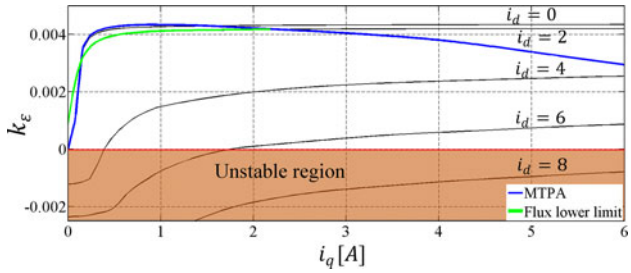

Fig. 10. Position error factor k_ϵ as a function of i_q, with i_d as parameter. MTPA (blue) and minimum excitation limit 0.7 Vs (green) are reported.

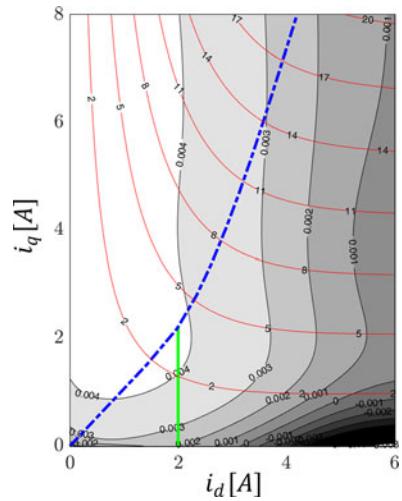

Fig. 11. Contour lines of k_ϵ in the i_d, i_q plane. Blue line is MTPA trajectory, green line is where the flux equals 0.7 Vs, black lines are k_ε contours, and red lines are torque contours [N·m].

Fig. 10. The MTPA trajectory (blue) and the flux lower limit (green) are also represented in Fig. 11, where k_ϵ contours are represented in the i_d, i_q plane. As can be seen, with adopted flux lower limitation, sign of k_ϵ does not change and is positive.

The bandwidth of tracking loop $\omega_{bw,HF}$ shown in Fig. 9 is as (21) where $k_{p,HF}$ is the proportional gain of PI regulator. In [24], the suggested bandwidth is three times smaller than the LPF cutoff frequency, as reported in

$$\omega_{bw,HF} = k_{p,HF} \cdot k_\epsilon\,(i_d, i_q) \leq \frac{1}{3}\omega_{bw,LPF}. \tag{21}$$

E. Fusion of Active Flux and HF-Injection Methods

The rotor speed estimation based on active flux method is computed in discrete form as in (22) where $\sin(\hat{\theta}_{AF})$ and $\cos(\hat{\theta}_{AF})$ are obtained from (11) and f_s is the sampling frequency in Hertz. Subscripts k and $k-1$ indicate the current time sample t_k and $t_k - T_s$, respectively

$$\hat{\omega}_{AF,k} = \left(\sin\hat{\theta}_{AF,k}\,\cos\hat{\theta}_{AF,k-1} - \cos\hat{\theta}_{AF,k}\,\sin\hat{\theta}_{AF,k-1}\right) \cdot f_s. \tag{22}$$

Position estimation based on active flux is combined with HF-injection-based technique as illustrated in Fig. 12. The gain k is intercalated to switch on and off the HF-injection loop. As can be seen, below 50 r/min, k is equal to 1. From 50 to

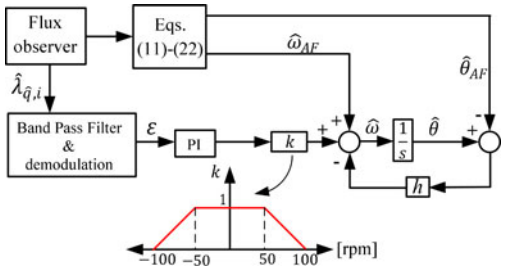

Fig. 12. Hybrid position and speed observer.

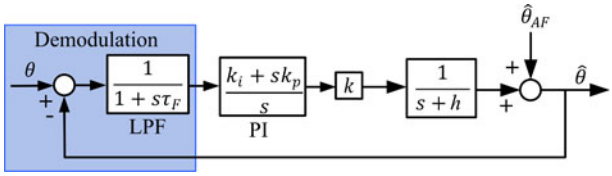

Fig. 13. Fusion structure, equivalent to the scheme of Fig. 12.

100 r/min, k decreases linearly and it is zero above 100 r/min. Also, the HF injection is dropped out according to the gain k. Therefore, above 100 r/min, position estimation is purely based on the AF method. Also, a pole h rad/s is inserted between observed position $\hat{\theta}$ and AF-based observed position $\hat{\theta}_{AF}$ for the sake of a smooth transition.

The active flux estimation is precise at medium and high speed and during the transients, while the injection is needed at low speed. For analysis purposes, the fusion structure of Fig. 12 is equivalent to the scheme presented in Fig. 13, where the cutoff frequency of LPF is 50 Hz. The transfer function related to the two angle estimations can be easily obtained as (23) and (24), where k_p and k_i are the proportional and integral gains of PI regulator shown in Fig. 13. It should be noted that $k_p = k_{p,HF} \cdot k_\epsilon$ and $k_i = k_{i,HF} \cdot k_\epsilon$. The values of k_p and k_i have been set at 120 and 5000, respectively. Also, h has been set at 25 rad/s

$$\begin{cases} \hat{\theta} = G_{HF} \cdot \theta + G_{AF} \cdot \hat{\theta}_{AF} \\ G_{HF} = \dfrac{H}{1+H} \\ G_{AF} = \dfrac{1}{1+H} \end{cases} \tag{23}$$

where H is the open-loop transfer function of the tracking loop

$$H = \frac{1}{1+s\tau_f} \cdot \frac{K_i + sK_p}{s} \cdot k \cdot \frac{1}{s+h}. \tag{24}$$

Fig. 14 illustrates the bode diagram of the two transfer functions at low speed where $k = 1$. As can be seen, the angle $\hat{\theta}$ is estimated based on the HF injection, while the information coming from active flux is used at HF, i.e., during the transients, where the contribution of the HF injection is negligible. In this way, a considerable bandwidth extension is achieved. Also, it is seen that the bandwidth of position estimation based on HF injection is around 16 Hz in steady state which is approximately three times smaller than the bandwidth of LPF. With increasing the speed above 50 r/min, and, thus, reducing

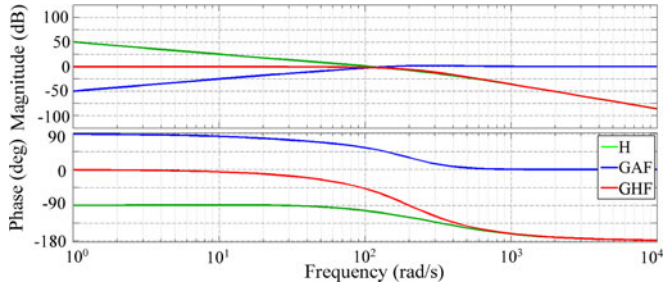

Fig. 14. Bode diagram of the proposed sensorless fusion structure.

the coefficient k, the open-loop characteristic (H) moves down, leading the crossover point to lower frequencies. It means that active-flux-based estimation will be active at lower frequencies, while the bandwidth of HF loop decreases gradually. At speeds above 100 r/min where $k = 0$, the observed angle simply comes from the active flux without additional filters ($\hat{\theta} = \hat{\theta}_{AF}$).

F. Criteria for Minimum Excitation Limit Selection

The key obstacle in using MTPA for encoderless control of pure SyR motors is the zero torque, zero current condition. At zero torque reference, the MTPA law for a SyR machine would command zero current ($i_d = 0$ and $i_q = 0$). In DFVC, this would mean using zero flux amplitude for zero torque ($\lambda^* = 0$).

Dealing with position estimation, such zero excitation condition is a critical one to those sensorless techniques based on back-EMF integration, because a SyR machine at zero current has no back EMF to track. Moreover, it is also critical for position detection based on HF injection and saliency tracking, since SyR machines have a singularity in the origin of the i_d, i_q plane. In other words, in SyR machines, the structural bridges are not saturated around zero current, and, thus, the incremental inductances in d- and q-axis are very similar, leading to low saliency, as evident from Fig. 2. This is also verified in Fig. 10, where the position error gain k_ε is almost null for $i_d = 0, i_q = 0$, standing for the low or zero saliency. As seen, if the MTPA law (blue line) is strictly adopted, the error gain k_ε reaches zero at zero i_d and i_q and saliency tracking becomes impossible. Conversely, the green line representing k_ε for $i_d = 2$ A is always above zero and this tells that the rotor position can be always estimated using saliency tracking. This is why below a certain reference torque, the condition $i_d = 2$ A (i.e., $\lambda^* = 0.7$ Vs) is used instead of the MPTA. Choosing a higher value of minimum excitation (e.g., $i_d > 2$ A), would shift the tracking loop to unstable region as shown in Fig. 10, for example, with $i_d = 4$ A: as can be observed, the k_ε gain has negative values for $i_d = 4$ A or more. Therefore, for this motor, $i_d = 2$ A, or 0.7 Vs, is the best candidate for guaranteeing saliency tracking at no load condition. This minimum excitation condition corresponds to circa 70% of nominal flux linkage, to say that it is also a significant level of excitation guaranteed to the back-EMF-based part of the flux and position observer.

It is worth mentioning that PM synchronous motors do not suffer from the aforementioned problems, because the PM produce back EMF also at zero current, and because they do not have the unsaturated bridges saliency issue at zero current.

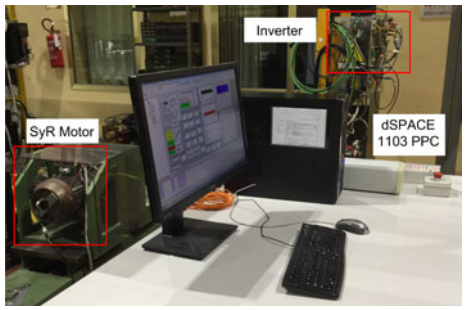

Fig. 15. Experimental test bench.

TABLE I
SYR MACHINE UNDER TEST SPECIFICATIONS

Rated power/Number of poles	2.2 kW/4
Nominal speed/rated torque	1500 r/min/14 N·m
Nominal current	7 A
Phase resistance	3.5 Ω
Moment of inertia (J)	$0.005\,\mathrm{kg}\cdot\mathrm{m}^2$
Max current (inverter limit)	20 A
Inverter voltage (dc-link)	520 V

IV. EXPERIMENTAL RESULTS

The effectiveness of the proposed sensorless DFVC method is investigated experimentally. A view of test rig is shown in Fig. 15. The controller is a dSPACE 1103 PPC board. The sampling and switching period is $T_s = 100\ \ \mu$s. A variable-speed drive with active front end (ABB Selivector) is used to impose the load torque or alternatively to set the speed in the tests. The rotor position is measured through a quadrature encoder with 512 cycles per revolution for monitoring purposes. The ratings of the SyR motor under test are reported in Table I.

A. Response of Closed-Loop Speed Control

The performance of the drive at standstill is depicted in Fig. 16. A 17-N·m step load (121% of rated torque) is applied to the motor at $t = 1.2$ s and removed at $t = 8.2$ s. Estimated and actual speed, estimated torque, current on q_s-axis, observed flux, position estimation error, and three-phase currents are shown in this figure. As can be seen, the position estimation error is very close to zero and dynamic response of the system is fairly good.

Results of a similar test run at 300 r/min with 17-N·m step load are presented in Fig. 17. The position estimation at this speed is purely based on AF method.

Fig. 18 shows the response to speed reference reversal in no-load condition, from $+10$ to -10 r/min. Again, the position estimation error is approximately zero and dynamic response of the system is acceptable. Also, the speed estimation is accurate. It should be commented that the residual noise on measured speed is due to the discretized position signal from encoder. The measured speed is calculated from the derivative of the position coming from a 512 cycles per revolution encoder and then LPF to reduce the quantization noise. Nevertheless, the quantization of the position produces relevant noise, more evident at low speed. Moreover, the measured speed contains fourth harmonic probably due to rotor mechanical defects. Estimated speed has

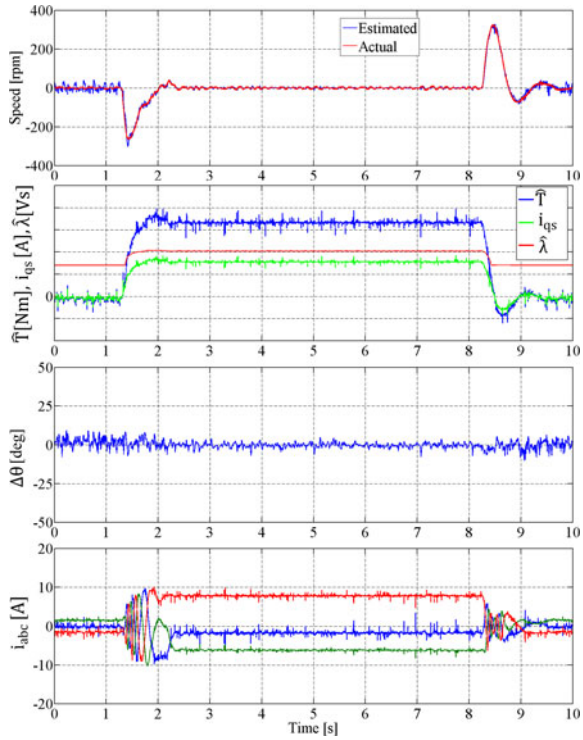

Fig. 16. Load steps at standstill: 0 to 17 N·m (121% of rated torque) and vice versa. Second figure from the top: blue: $\hat{T}$ (5 N·m/div); green: i_{qs} (3.5 A/div); red: $\hat{\lambda}$ (0.5 Vs/div).

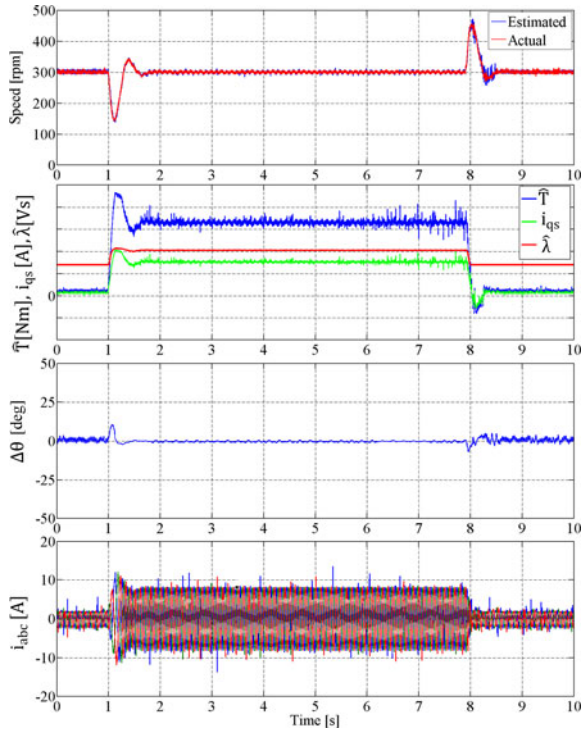

Fig. 17. Load steps at 300 r/min: 17-N·m (121% of rated torque) loading. Second figure from the top: blue: $\hat{T}$ (5 N·m/div); green: i_{qs} (3.5 A/div); red: $\hat{\lambda}$ (0.5 Vs/div).

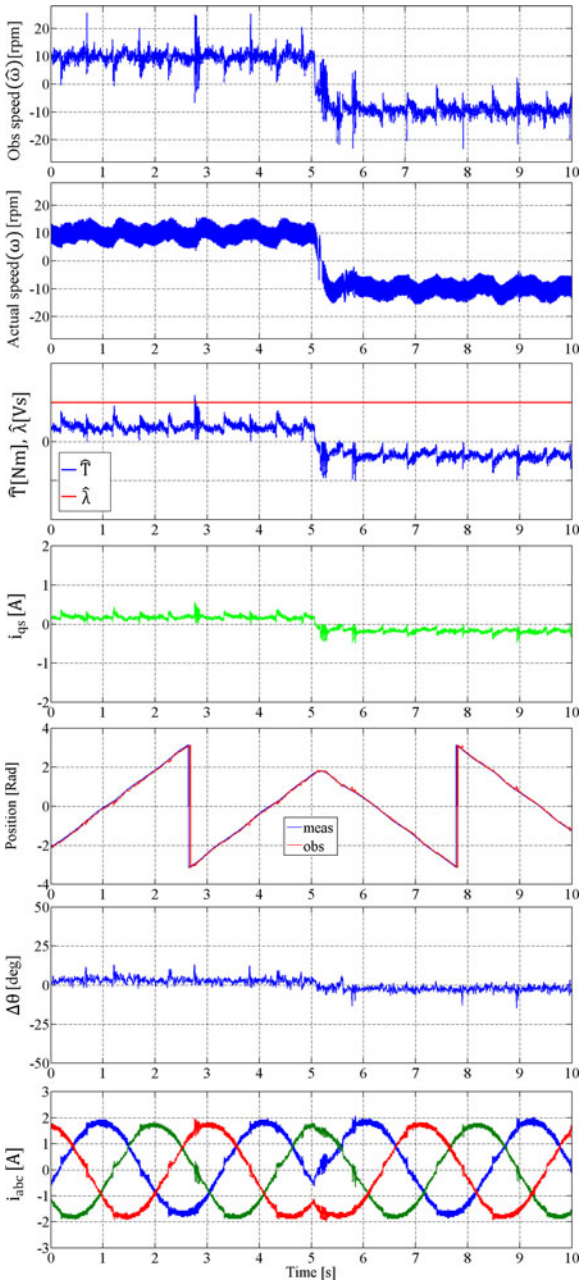

Fig. 18. No-load speed reversal from 10 to -10 r/min. Third figure from the top: blue: $\hat{T}$ (1 N·m/div); red: $\hat{\lambda}$ (0.7 Vs/div).

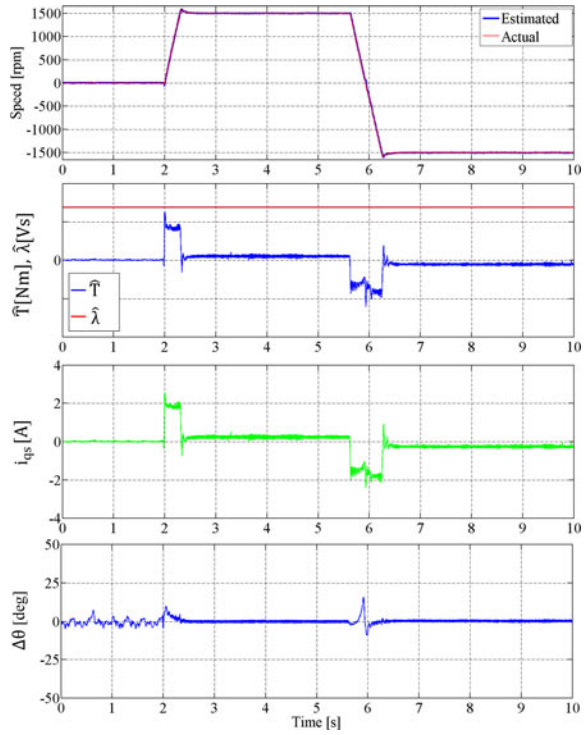

Fig. 19. No-load high-speed reversal from $0 \rightarrow 1500 \rightarrow -1500$ r/min. Second figure from the top: blue: $\hat{T}$ (5 N·m/div); red: $\hat{\lambda}$ (0.5 Vs/div).

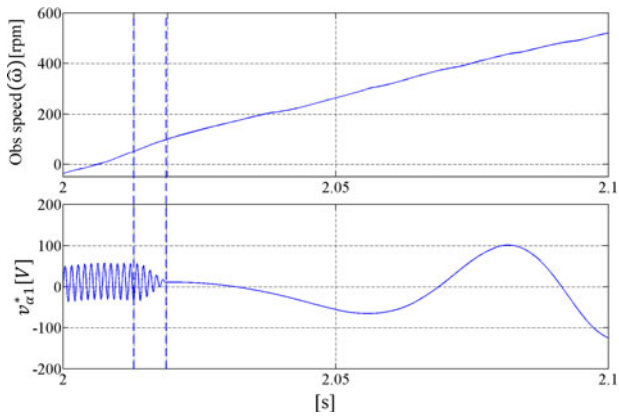

Fig. 20. HF injection and dropping out methodology: Zoom of estimated speed and $v^*_{\alpha 1}$.

the same noise components of measured speed, plus a sixth harmonic residual oscillation due to nonperfectly compensated of inverter nonlinear errors.

B. Transition Between the Two Sensorless Models

To investigate the performance of the proposed method during transition between low-speed and high-speed regions, motor is commanded to 1500 r/min at $t = 2$ s and again to -1500 r/min at $t = 5.9$ s as illustrated in Fig. 19. It is seen that the position estimation error is around zero in steady states and acceptable during transients.

As said, the HF injection starts to decrease gradually above 50 r/min and is completely dropped out above 100 r/min. To validate this, estimated speed and $v^*_{\alpha 1}$ (see Fig. 4) have been magnified in Fig. 20.

C. Flux Weakening

Fig. 21 reports the FW test where the speed travels to 3000 r/min at $t = 0.8$ s and again decelerates and goes to -3000 r/min at $t = 5$ s. As can be seen, above 2000-r/min machine goes to FW region according to (7). From torque, i_{qs}, and flux waveforms, it is seen that in the range of 2000–3000 r/min, flux is decreasing and conversely i_{qs} increases to deliver a constant

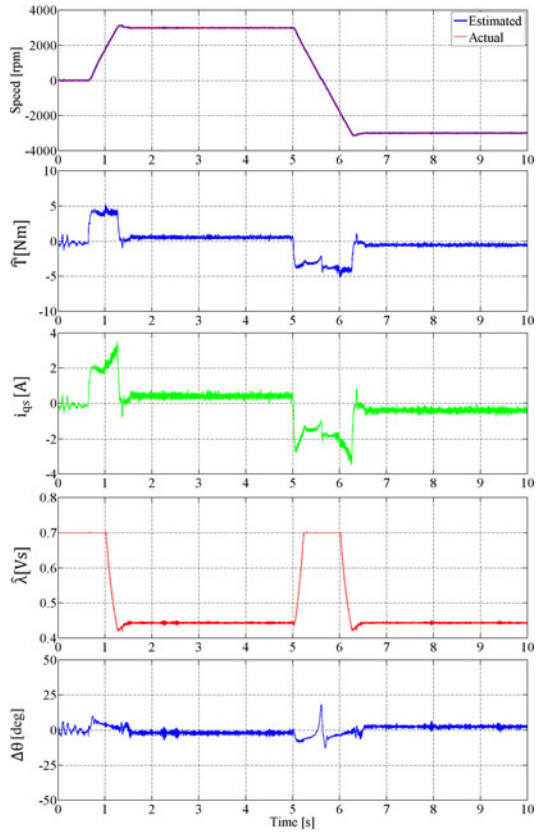

Fig. 21. FW test from $0 \rightarrow 3000 \rightarrow -3000$ r/min.

torque. Also, the position estimation error is zero at steady state and is limited during transients. The FW block reduces the flux amplitude below the minimum excitation value (0.7 Vs), to comply with the voltage constraint.

D. Cross Saturation Error

As said in Section III-B, provided that in the proposed sensorless technique HF component of $\hat{\lambda}_{\hat{q},i}$ signal is demodulated in place of current component, the cross saturation effect is inherently overcome. To verify that positive and negative 14-N·m ramp torque reference is applied to the motor while the shaft is kept at standstill using the speed-controlled load. As can be seen from Fig. 22, while the applied command torque is ramping up and down, rotor position estimation error is close to zero. The same test has been done using demodulation of current on estimated $\hat{q}$-axis, according to [24]. As can be seen in Fig. 23, during torque ramping, the position estimation errors ramps up and down due to cross saturation effect. In order to compensate this effect, demodulation technique should be modified as (25), [24]. As can be seen, (25) is motor parameter dependent and is prone to produce error when motor parameters vary according to different working points. While, the demodulation process used in this paper is independent of motor parameters

$$\epsilon_{[24]} = \mathrm{LPF}\left(\frac{L_{dq}}{L_{qq}} \cdot I_{\hat{d}HF} + I_{\hat{q}HF}\right) \cdot \sin\left(\omega_c t\right). \qquad (25)$$

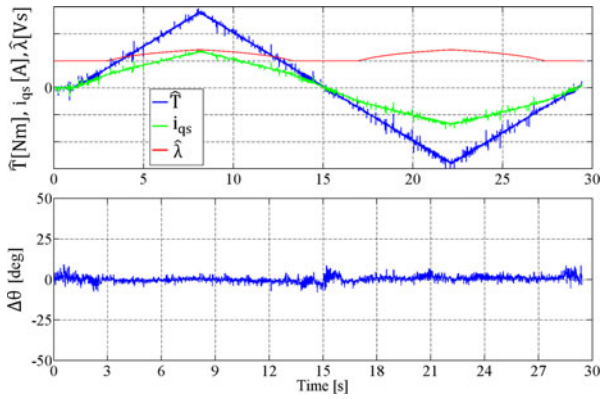

Fig. 22. Torque control test at standstill: 14-N·m load ramp is applied when $\hat{\lambda}_{\hat{q},i}$ signal is demodulated (proposed demodulation). Top figure, blue: $\hat{T}$ (5 N·m/div); green: i_{qs} (3.5 A/div); red: $\hat{\lambda}$ (0.7 Vs/div).

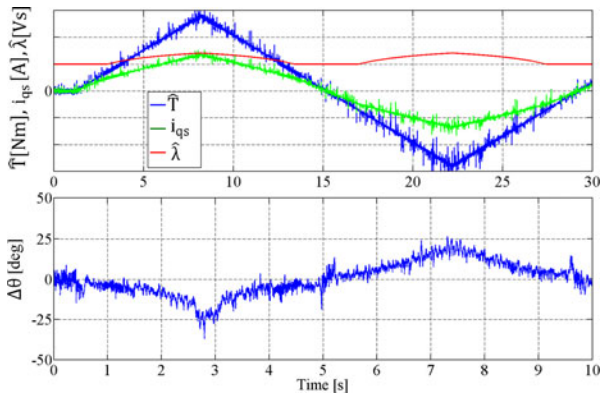

Fig. 23. Torque control test at standstill: 14-N·m load ramp is applied when $\hat{q}$-axis current is demodulated. Top figure, blue: $\hat{T}$ (5 N·m/div); green: i_{qs} (3.5 A/div); red: $\hat{\lambda}$ (0.7 Vs/div).

V. Conclusion

A sensorless technique based on a direct-flux vector control has been presented for SyR motor drives. The proposed hybrid position estimation technique uses the fusion of active flux estimation and pulsating HF voltage injection. Flux demodulation technique is used instead of standard quadrature current demodulation for tracking the rotor position at zero and low speeds, inherently compensating for the effects of cross saturation. Moreover, an extensive analysis has been done in peculiarities of pure SyR motors around zero torque in sensorless controls. Based on this analysis, a minimum flux limit with MTPA strategy has been proposed. The feasibility of the proposed control method is demonstrated in experiments. The reported results show the good dynamic response at different speed and torque levels and the zero steady-state position error. Position error during speed transients is under control. The transition between the two sensorless models is seamless in both acceleration and deceleration. Finally, the FW speed range is easily exploited thanks to the natural predisposition of the proposed DFVC technique. The proposed control technique is a good candidate for general purpose sensorless control of SyR motor drives.

REFERENCES

[1] A. Vagati, M. Pastorelli, and G. Franceschini, "High-performance control of synchronous reluctance motors," *IEEE Trans. Ind. Appl.*, vol. 33, no. 4, pp. 983–991, Jul./Aug. 1997.

[2] B-H. Bae and S-K. Sul, "A novel dynamic overmodulation strategy for fast torque control of high-saliency-ratio AC motor," *IEEE Trans. Ind. Appl.*, vol. 41, no. 4, pp. 1013–1019, Jul./Aug. 2005.

[3] S. Taghavi and P. Pillay, "A novel grain-oriented lamination rotor core assembly for a synchronous reluctance traction motor with a reduced torque ripple algorithm," *IEEE Trans. Ind. Appl.*, vol. 52, no. 5, pp. 3729–3738, Sep./Oct. 2016.

[4] Y. Inoue, S. Morimoto, and M. Sanada, "Comparative study of PMSM drive systems based on current control and direct torque control in flux-weakening control region," *IEEE Trans. Ind. Appl.*, vol. 48, no. 6, pp. 2382–2389, Nov./Dec. 2012.

[5] A. Yousefi-Talouki, S. A. Gholamian, M. Yousefi-Talouki, R. Ilka, and A. Radan, "Harmonic elimination in switching table-based direct torque control of five-phase PMSM using matrix converter," in *Proc. 2012 IEEE Symp. Humanities, Sci. Eng. Res.*, Kuala Lumpur, Malaysia, 2012, pp. 777–782.

[6] G. Foo, S. Sayeef, and M. F. Rahman, "Low-speed and standstill operation of a sensorless direct torque and flux controlled IPM synchronous motor drive," *IEEE Trans. Energy Convers.*, vol. 25, no. 1, pp. 25–33, Mar. 2010.

[7] A. Tripathi, A. M. Khambadkone, and S. K. Panda, "Torque ripple analysis and dynamic performance of a space vector modulation based control method for AC-drives," *IEEE Trans. Power Electron.*, vol. 20, no. 2, pp. 485–492, Mar. 2005.

[8] G. Pellegrino, R. I. Bojoi, and P. Guglielmi, "Unified direct-flux vector control for AC motor drives," *IEEE Trans. Ind. Appl.*, vol. 47, no. 5, pp. 2093–2102, Sep./Oct. 2011.

[9] G. Pellegrino, E. Armando, and P. Guglielmi, "Direct-flux vector control of IPM motor drives in the maximum torque per voltage speed range," *IEEE Trans. Ind. Electron.*, vol. 59, no. 10, pp. 3780–3788, Oct. 2012.

[10] G. Pellegrino, B. Boazzo, and T. M. Jahns, "Plug-in direct-flux vector control of PM synchronous machine drives," *IEEE Trans. Ind. Appl.*, vol. 51, no. 5, pp. 3848–3857, Sep./Oct. 2015.

[11] Y. Zhao, W. Qiao, and L. Wu, "Improved rotor position and speed estimators for sensorless control of interior permanent-magnet synchronous machines," *IEEE J. Emerging Sel. Topics Power Electron.*, vol. 2, no. 3, pp. 627–639, Sep. 2014.

[12] Y. Zhao, W. Qiao, and L. Wu, "An adaptive quasi-sliding-mode rotor position observer-based sensorless control for interior permanent magnet synchronous machines," *IEEE Trans. Power Electron.*, vol. 28, no. 12, pp. 5618–5629, Dec. 2013.

[13] G. H. B. Foo and M. F. Rahman, "Direct torque control of an IPM-synchronous motor drive at very low speed using a sliding-mode stator flux observer," *IEEE Trans. Power Electron.*, vol. 25, no. 4, pp. 933–942, Apr. 2010.

[14] J. Holtz, "Acquisition of position error and magnet polarity for sensorless control of PM synchronous machines," *IEEE Trans. Ind. Appl.*, vol. 44, no. 4, pp. 1172–1180, Jul./Aug. 2008.

[15] A. Piippo and J. Luomi, "Adaptive observer combined with HF signal injection for sensorless control of PMSM drives," in *Proc. 2005 IEEE Int. Conf. Electr. Mach. Drives*, San Antonio, TX, USA, 2005, pp. 674–681.

[16] O. Wallmark and L. Harnefors, "Sensorless control of salient PMSM drives in the transition region," *IEEE Trans. Ind. Electron.*, vol. 53, no. 4, pp. 1179–1187, Jun. 2006.

[17] Z. Ma, J. Gao, and R. Kennel, "FPGA implementation of a hybrid sensorless control of SMPMSM in the whole speed range," *IEEE Trans. Ind. Informat.*, vol. 9, no. 3, pp. 1253–1261, Aug. 2013.

[18] G. Andreescu, C. I. Pitic, F. Blaabjerg, and I. Boldea, "Combined flux observer with signal injection enhancement for wide speed range sensorless direct torque control of IPMSM drives," *IEEE Trans. Energy Convers.*, vol. 23, no. 2, pp. 393–402, Jun. 2008.

[19] D. Nguyen, R. Dutta, M. F. Rahman, and J. E. Fletcher, "Performance of a sensorless controlled concentrated-wound interior permanent-magnet synchronous machine at low and zero speed," *IEEE Trans. Ind. Electron.*, vol. 63, no. 4, pp. 2016–2026, Apr. 2016.

[20] I. Boldea, M. C. Paicu, G. D. Andreescu, and F. Blaabjerg, "Active flux" DTFC-SVM sensorless control of IPMSM," *IEEE Trans. Energy Convers.*, vol. 24, no. 2, pp. 314–322, Jun. 2009.

[21] I. Boldea *et al.*, "DTFC-SVM motion-sensorless control of a PM-assisted reluctance synchronous machine as starter-alternator for hybrid electric vehicles," *IEEE Trans. Power Electron.*, vol. 21, no. 3, pp. 711–719, May 2006.

[22] R. Morales-Caporal and M. Pacas, "Encoderless predictive direct torque control for synchronous reluctance machines at very low and zero speed," *IEEE Trans. Ind. Electron.*, vol. 55, no. 12, pp. 4408–4416, Dec. 2008.

[23] S.-C. Agarlita, I. Boldea, and F. Blaabjerg, "High-frequency-injection-assisted "active-flux"-based sensorless vector control of reluctance synchronous motors, with experiments from zero speed," *IEEE Trans. Ind. Appl.*, vol. 48, no. 6, pp. 1931–1939, Nov./Dec.2012.

[24] T. Tuovinen and H., M, "Adaptive full-order observer with high-frequency signal injection for synchronous reluctance motor drives," *IEEE J. Emerging Sel. Topics Power Electron.*, vol. 2, no. 2, pp. 181–189, Jun. 2014.

[25] F. J. W. Barnard, W. T. Villet, and M. J. Kamper, "Hybrid active-flux and arbitrary injection position sensorless control of reluctance synchronous machines," *IEEE Trans. Ind. Appl.*, vol. 51, no. 5, pp. 3899–3906, Sep./Oct. 2015.

[26] R. Bojoi, P. Guglielmi, and G. Pellegrino, "Sensorless stator field-oriented control for low cost induction motor drives with wide field weakening range," in *Proc. 2008 IEEE Ind. Appl. Soc. Annu. Meet.*, Oct. 5–9, 2008, pp. 1–7.

[27] A. Yousefi-Talouki and G. Pellegrino, "Sensorless direct flux vector control of synchronous reluctance motor drives in a wide speed range including standstill," in *Proc. 2016 XXII Int. Conf. Electr. Mach. (ICEM)*, Lausanne, Switzerland, 2016, pp. 1167–1173.

[28] M. Hinkkanen, P. Pescetto, E. Mölsä, S. E. Saarakkala, G. Pellegrino, and R. Bojoi, "Sensorless self-commissioning of synchronous reluctance motors at standstill," in *Proc. 2016 XXII Int. Conf. Electr. Mach.*, Lausanne, Switzerland, 2016, pp. 1174–1180.

[29] I. Boldea, M. C. Paicu, and G. Andreescu, "Active flux concept for motion-sensorless unified AC drives," *IEEE Trans. Power Electron.*, vol. 23, no. 5, pp. 2612–2618, Sep. 2008.

[30] P. Guglielmi, M. Pastorelli, and A. Vagati, "Impact of cross-saturation in sensorless control of transverse-laminated synchronous reluctance motors," *IEEE Trans. Ind. Electron.*, vol. 53, no. 2, pp. 429–439, Apr. 2006.

Arzhang Yousefi-Talouki received the Bachelor's degree in electrical engineering from the University of Mazandaran, Babolsar, Iran, in 2009, and the Master's degree in electrical engineering from Babol University of Technology, Babol, Iran, in 2012. He is currently working toward the Ph.D. degree in electrical engineering at Plotecnico di Torino, Turin, Italy.

His current research interests include electrical machine drives, especially synchronous motor drives and sensorless control.

Paolo Pescetto received the Bachelor's and Master's degrees (full grade and Hons.) in electrical engineering from Politecnico di Torino, Turin, Italy, in 2013 and 2015, respectively, where he is currently working toward the Ph.D. degree in electrical engineering.

In 2014, he has been an Erasmus+ student with the Norwegian University of Science and Technology, Trondheim, Norway. His current research interests include synchronous motor drives, sensorless control, and self-commissioning techniques.

Gianmario Pellegrino (M'06–SM'13) received the M.Sc. and Ph.D. degrees in electrical engineering from the Politecnico di Torino, Turin, Italy, in 1998 and 2002, respectively.

He was a Visiting Scholar with Aalborg University, Denmark, with the University of Nottingham, U.K., and with the University of Wisconsin-Madison, USA. He is currently an Associate Professor with the Politecnico di Torino. He is involved in research projects with industry and has 30 journal papers and one patent. His research interests include the design of electrical machines and the control of electrical drives.

Dr. Pellegrino is an Associate Editor for the IEEE TRANSACTIONS ON INDUSTRY APPLICATIONS. He is the corecipient of six Prize Paper Awards.

Ion Boldea (M'77–SM'81–F'96–LF'14) received the M.S. and Ph.D. degrees in electrical engineering from the Politehnica University of Timisoara, Timisoara, Romania, in 1967 and in 1973, respectively.

He is currently a Full Professor with the Politehnica University of Timisoara. He has worked and published extensively in linear and rotary electric machines, drives, and magnetic levitation vehicles. He has published numerous books, with 6000 entrances in libraries worldwide.

Dr. Boldea is a member of the Industrial Drives Committee and the Electric Machines Committee of the IEEE Industry Applications Society (IAS). He has been the Chairman of the OPTIM International Conferences (IEEE-IAS sponsored) from 1996 to present. He received the 2015 IEEE Nikola Tesla Award.